ROYAL SOCIETY
OF CHEMISTRY

PAPER

Check for updates

A penta-BCP sheet with strong piezoelectricity and a record high positive Poisson's ratio†

Changsheng Hou, Yiheng Shen, Wei Sun, Yanyan Chen, Dongyuan Ni and Qian Wang [ID] *

Two-dimensional structures composed solely of pentagonal motifs are of particular interest due to their unique geometries and novel properties. In particular, the broken centrosymmetry in many pentagon-based sheets results in piezoelectricity. Herein, we rationally design a penta-BCP sheet with large intrinsic polarization and weak mechanical strength. First-principles calculations reveal that the penta-BCP sheet is a dynamically, thermally, and mechanically stable semiconductor with an indirect band gap of 2.97 eV. More interestingly, the penta-BCP sheet is found to be the first penta-sheet with a positive Poisson's ratio larger than 1.00 (1.30), and possesses prominent spontaneous polarization ($P_s = 4.66 \times 10^{-10}$ C m^{-1}) and piezoelectricity ($d_{21} = -13.57$ pm V^{-1}, and $d_{22} = 6.33$ pm V^{-1}). The large positive Poisson's ratio coupled with its piezoelectricity leads to a significant overall piezoelectric response of 24 pm V^{-1}. This study expands the family of ternary pentagon-based sheets with outstanding properties.

1. Introduction

Piezoelectric materials exhibit tunable electrical polarization under mechanical strain, enabling the conversion between electrical and mechanical energy. In principle, these materials should be non-centrosymmetric and non-metallic. They are widely used in applications like functional sensors, nano-sized actuators, and energy harvesters. In recent years, two-dimensional (2D) piezoelectric materials have received extensive attention, primarily because spontaneous polarization and piezoelectricity at the nanoscale are expected to realize device miniaturization.[1,2] Moreover, many centrosymmetric 3D bulk materials break their inversion symmetry when thinned down to 2D materials, providing more opportunities to form spontaneous polarization and generate piezoelectricity.[3] However, spontaneous polarization and the piezoelectric response are rarely seen in conventional 2D materials that consist of hexagonal motifs due to the centrosymmetry of their geometries.[4] To overcome this problem, pentagons are used to construct 2D materials. Since the theoretical prediction of penta-graphene in 2015,[5] 2D materials composed of pure pentagonal motifs have attracted much attention,[6–10] and some pentagon-based 2D materials have been experimentally synthesized, including penta-silicene nanoribbons,[11] penta-PdSe$_2$,[12] and penta-NiN$_2$.[4] Numerous penta-sheets can exhibit exceptional piezoelectric

properties.[13–17] For example, although graphene exhibits no piezoelectricity, penta-graphene is piezoelectric.[15] Meanwhile, piezoelectricity is a general property of the semiconducting penta-graphene-like structures because they are all non-centrosymmetric with the space group symmetry of $P\bar{4}2_1m$.[18] In addition, spontaneous polarization can be introduced in penta-sheets with enhanced piezoelectric responses. For instance, the out-of-plane spontaneous polarization has been found in hydrofluorinated penta-graphene,[13] penta-CoAsS,[14] and penta-CCB[15] due to the asymmetry along the out-of-plane direction. By contrast, in-plane spontaneous polarization can also be introduced through a small tilt of the Si–Si dimers[19] or the existence of B–N or P–N polarized bonds.[16,17] From the physics point of view, the polarized bonds and mechanical strengths of pentagon-based sheets significantly impact their spontaneous polarization and piezoelectric response.[20] However, in these reports, the coupling between the individual piezoelectric coefficients was neglected,[21] which actually may play an important role when the Poisson's ratio is large.[22] Hence, an intriguing question arises: can we design a ternary pentagon-based piezoelectric sheet with a large Poisson's ratio and a significant piezoelectric response?

To answer this question, it is important to note the facts that the electron cloud of sp^2-B atoms is not easily deformed,[23] and the related bond lengths and bond angles are not easily changed. By contrast, the electron cloud of P atoms is relatively easy to deform,[24] and the related bond lengths and bond angles are relatively flexible, resulting in weak mechanical strength. These factors, together with the flexible bonding of C, provide the basis for a B–C–P penta-sheet with a promising

School of Materials Science and Engineering, CAPT, Peking University, Beijing 100871, China. E-mail: qianwang2@pku.edu.cn

† Electronic supplementary information (ESI) available. See DOI: **https://doi.org/10.1039/d2tc02053j**

piezoelectric performance. In addition, because the electronegativity of the P atom is between that of C and B atoms, the C–B bonds should be highly polarized and can enhance spontaneous polarization when coincided with the polarized direction of the pentagon-based sheet. Thus, it can be expected that this BCP ternary pentagon-based sheet possesses a large piezoelectric response. This motivates us to carry out this study.

2. Computational methods

Calculations within the framework of density functional theory (DFT) are performed utilizing the Vienna *ab initio* simulation package (VASP).[25] The projector augmented wave (PAW) method[26] is used to treat the interactions between valence electrons and ion cores. Plane waves with a kinetic energy cutoff of 600 eV are used to expand the wavefunction of the valence electrons. The exchange–correlation interaction of electrons prescribed by the Perdew–Burke–Ernzerhof (PBE) functional[27] within the generalized gradient approximation (GGA) is used in geometry optimization and properties calculations, while the hybrid Heyd–Scuseria–Ernzerhof (HSE06) functional[28] is used for more accurate electronic structure calculations. For geometry optimization, the convergence criteria for the total energy and atomic force components are set to 10^{-8} eV and 10^{-6} eV Å^{-1}, respectively. The first Brillouin zone is represented by a $9 \times 9 \times 1$ k-point grid using the Monkhorst–Pack scheme.[29] The vacuum space is set to 17.7 Å to avoid the interactions between the periodic images. The finite displacement method[30] implemented in the Phonopy code[31] is used for phonon spectra calculations using a $5 \times 5 \times 1$ supercell of penta-BCP. In *ab initio* molecular dynamics (AIMD) simulations,[32] the canonical ensemble with a Nosé thermostat[33] is used to realize temperature control. The elastic constants are calculated using finite difference methods.[34] The spontaneous polarization is quantified using the finite electric field method based on Berry phase theory.[35] The piezoelectric

tensor coefficients are obtained using density functional perturbation theory (DFPT)[36] as implemented in VASP.

3. Results and discussion

3.1 Structure and stability

The optimized structure of penta-BCP is presented in Fig. 1(a), which possesses $P2_1$ symmetry (space group no. 4). The unit cell contains two B, two C, and two P atoms, which occupy three non-equivalent Wyckoff positions, namely, $2a_1$ (0.879, 0.861, 0.526), $2a_2$ (0.773, 0.508, 0.507), and $2a_3$ (0.538, 0.186, 0.562), respectively. The lattice parameters of penta-BCP are $a = 3.67$ Å and $b = 4.12$ Å. The top view shows that the penta-BCP sheet is composed exclusively of pentagons consisting of B, C, and P atoms. The C–B, C–P, and B–P bond lengths are 1.56, 1.92, and 1.96 Å, respectively. The buckling height of this structure is 2.47 Å, which is larger than that of ternary penta-BCN (1.34 Å)[16] and penta-CNP (2.41 Å)[17] due to the larger bond lengths of penta-BCP compared with penta-BCN and penta-CNP. The coordinates and lattice parameters of the optimized geometry are listed in the ESI.† To identify the chemical stability of penta-BCP, we calculate the cohesive energy (E_{coh}) of penta-BCP, which is defined as $E_{coh} = (E_{\text{penta-BCP}} - 2E_B - 2E_C - 2E_P)/6$, where E_B, E_C, E_P, and $E_{\text{penta-BCP}}$ represent the energy of an isolated B atom, C atom, P atom, and a unit cell of penta-BCP, respectively. The resulting cohesive energy of penta-BCP is -5.61 eV per atom, which is comparable to that of many other ternary monolayers such as penta-BNSi (-5.43 eV per atom),[37] penta-SiCN (-4.36 eV per atom),[38] BPC$_2$ (-5.77 eV per atom),[39] and BiPbC$_3$ (-5.62 eV per atom),[40] indicating its energetic stability. We also calculate the formation energy (E_{form}) of penta-BCP (E_{form}) defined as: $E_{form} = (E_{\text{penta-BCP}} - 2E_s^B - 2E_s^C - 2E_s^P)/6$, where E_s^B, E_s^C, and E_s^P represent the energy of each B, C, and P atom in its most stable bulk phase, respectively. The calculated formation energy of penta-BCP is 0.09 eV per atom, implying that the procedure of synthesizing penta-BCP *via* the corresponding elementary substances is endothermic.
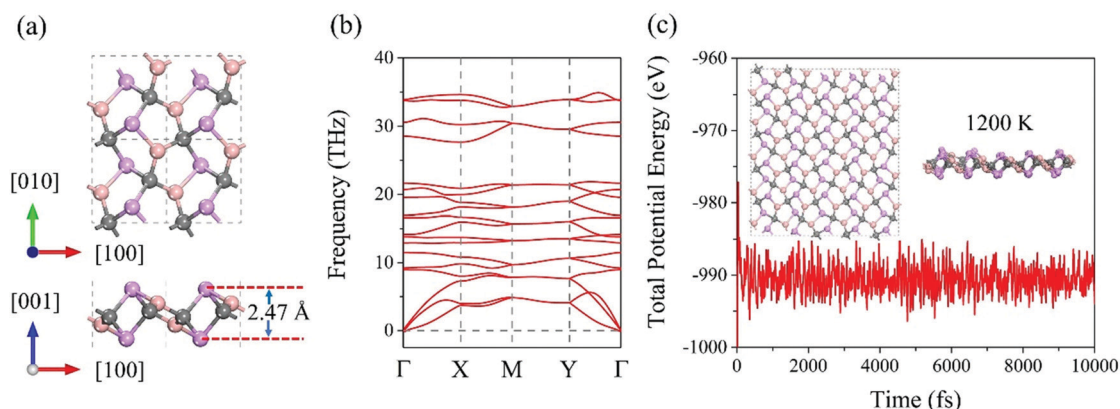

Fig. 1 (a) Top and side views, and (b) the phonon spectrum of penta-BCP. (c) Potential energy fluctuation with time during the AIMD simulation at 1200 K. The insets show snapshots of the atomic configuration of penta-BCP at the end of the simulation. The pink, gray, and purple spheres represent B, C, and P atoms, respectively.

This journal is © The Royal Society of Chemistry 2022

J. Mater. Chem. C, 2022, **10**, 10302–10309 | **10303**

The dynamic stability of penta-BCP is verified through calculating its phonon spectrum. As shown in Fig. 1(b), the absence of imaginary modes in the first Brillouin zone confirms that penta-BCP is dynamically stable. The thermal stability of penta-BCP is investigated by performing AIMD simulations at several different temperatures from 300 K to 1200 K at intervals of 300 K. The duration of each simulation is 10 ps with a time step of 1 fs. To avoid the fake stability caused by the constraints of periodic boundary conditions, a $5 \times 5 \times 1$ supercell is used in these simulations. The results obtained at 1200 K are plotted in Fig. 1(c), which shows that the total potential energy of the supercell fluctuates around a constant during the simulation at 1200 K, and the geometry of penta-BCP does not suffer significant distortion at the end of the simulation. The results from simulations at other temperatures are given in Fig. S1 in the ESI.† The thermal stability is also studied by calculating the change in Gibbs energy of penta-BCP with temperature. The Gibbs energy $G(T, p)$ is defined as $G(T,p) = \min_{V}\left[U(V) + F_{\text{phonon}}(T;V) + pV\right]$, where the right-hand side of this equation aims to find a minimum value for the contents of the square brackets by changing the volume (V), where $U(V)$ is the internal energy, $F_{\text{phonon}}(T;V)$ is the sum of phonon Helmholtz free energy, T is the temperature, and p is the pressure. Besides, $F_{\text{phonon}}(T;V)$ can be presented as $F_{\text{phonon}}(T;V) = \sum_{i=1}^{3N}\frac{\hbar\omega_i}{2} + \sum_{i=1}^{3N} kT \ln(1 - e^{-\hbar\omega_i/kT})$, where $3N$ represents the number of phonons, ω_i corresponds to the frequency of the phonon, $\hbar$ is the Dirac constant, and k is the Boltzmann constant. Using the quasi-harmonic approximation method[41] as implemented in Phonopy,[31] we obtain the change in Gibbs energy of penta-BCP with temperature as shown in Fig. S2 in the ESI.† For comparison, a similar calculation is also carried out for diamond, and both show similar behavior, further confirming the thermal dynamic stability of the penta-BCP sheet at finite temperatures. Finally, we examine the mechanical stability of this structure. The calculated linear elastic constants are $C_{11} = 47.49$ N m^{-1}, $C_{22} = 153.08$ N m^{-1}, $C_{12} = 61.81$ N m^{-1} and $C_{66} = 76.04$ N m^{-1}, which fully satisfy the Born–Huang criteria for this 2D material ($C_{11} > 0$, $C_{22} > 0$, $C_{66} > 0$, and $C_{11}C_{22} > C_{12}{}^2$),[42] confirming that penta-BCP is mechanically stable.

3.2 Mechanical properties

The mechanical properties of penta-BCP are investigated based on the calculated linear elastic constants. The in-plane Young's moduli E_{a} and E_{b} along the [100] and [010] directions are derived from the formula of $E_{\text{a}} = (C_{11}C_{22} - C_{12}{}^2)/C_{22}$ and $E_{\text{b}} = (C_{11}C_{22} - C_{12}{}^2)/C_{11}$, which are 22.65 N m^{-1} and 73.35 N m^{-1}, respectively. Accordingly, the in-plane Poisson's ratio $1 = C_{12}/C_{22}$ and $\nu_2 = C_{12}/C_{11}$ are, respectively, calculated to be 0.40 and 1.30. Using the following formulas,[43] we calculate the in-plane Young's modulus (E) and Poisson's ratio (ν) along an arbitrary direction (θ):

$$E(\theta) = \frac{C_{11}C_{22} - C_{12}{}^2}{C_{11}s^4 + C_{22}c^4 + \left(\frac{C_{11}C_{22} - C_{12}{}^2}{C_{66}} - 2C_{12}\right)c^2s^2} \quad (1)$$

$$\nu(\theta) = -\frac{\left(C_{11} + C_{22} - \frac{C_{11}C_{22} - C_{12}{}^2}{C_{66}}\right)c^2s^2 - C_{12}(c^4 + s^4)}{C_{11}s^4 + C_{22}c^4 + \left(\frac{C_{11}C_{22} - C_{12}{}^2}{C_{66}} - 2C_{12}\right)c^2s^2} \quad (2)$$

Here, $s = \sin\theta$, $c = \cos\theta$, and θ represents the in-plane angle with respect to the [100] direction. As shown in Fig. 2, the Young's modulus and Poisson's ratio of penta-BCP both exhibit similar butterfly-like characteristics, indicating the mechanical anisotropy of penta-BCP. One can see that the values of Young's modulus vary from 22.65 N m^{-1} to 167.88 N m^{-1}. The maximum is found for $\theta = 56°$, while the minimum is found for $\theta = 0°$. Note that the Young's moduli of penta-BCP are comparable to those of black phosphorene (23.0–92.3 GPa).[44] By contrast, they are smaller than those of penta-BCN (189–223 N m^{-1}),[16] penta-CNP (172–190 N m^{-1}),[17] penta-BNSi (109–113 N m^{-1}),[37] and penta-SiCN (129.88–131.29 N m^{-1}),[38] and they are much smaller compared with those of some common 2D materials such as graphene (340 N m^{-1}),[45] h-BN (275.8 N m^{-1}),[42] and MoS$_2$ (180 N m^{-1}),[46] suggesting that penta-BCP possesses weak
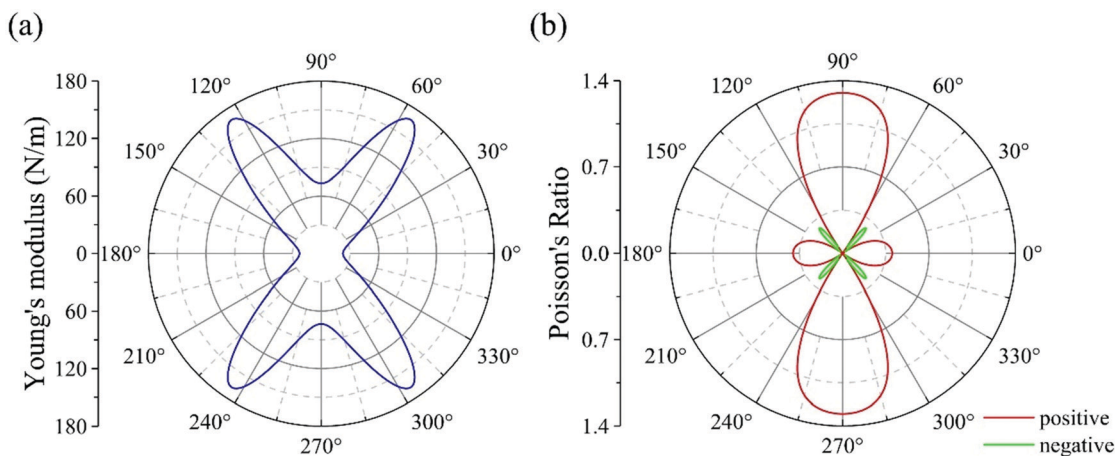

Fig. 2 Variation of (a) the in-plane Young's modulus, and (b) Poisson's ratio with the direction in penta-BCP.

10304 | *J. Mater. Chem. C*, 2022, **10**, 10302–10309

This journal is © The Royal Society of Chemistry 2022

mechanical strength. Therefore, it can be expected that penta-BCP could possess larger piezoelectric coefficients than penta-BCN and penta-CNP.

Interestingly, penta-BCP is the first pentagon-based sheet so far with a Poisson's ratio larger than 1.00. As shown in Fig. 2(b), penta-BCP exhibits a large positive Poisson's ratio of 1.30 along the [010] direction. To further confirm the large positive Poisson's ratio of penta-BCP, we identify the lateral strain in the [010] direction under a tensile strain of 1.0% along the [100] direction by finding the minimum total potential energy. The minimum of total potential energy is found at the lateral compressive strain of 0.4%, as shown in Fig. 3(a). Similarly, the lateral compressive strain is 1.25% along the [100] direction when a tensile strain of 1.0% is applied along the [010] direction. The calculated Poisson's ratios along the [100] and [010] directions based on the applied tensile strain and lateral compressive strain are 0.40 and 1.25, respectively, in agreement with the above results obtained based on the elastic constants. To further understand the large positive Poisson's ratio, we calculate the changes in bond angles centered at C with B_1/P_1 and B_2/P_2 for the B/P atoms above and below the carbon atoms, respectively, as illustrated in Fig. S3 in the ESI.† The values of $\theta_1(B_1–C–P_1)$ and $\theta_2(B_2–C–P_2)$ in the equilibrium state are 128.46° and 108.45°, respectively. After applying a tensile strain of 1% along the [010] direction, $\theta_1(B_1–C–P_1)$ decreases to 127.60°, while $\theta_2(B_2–C–P_2)$ increases to 109.78°, leading to a ratio of $-(\Delta x_2/x)/(\Delta y_2/y) = 1.10$, larger than 1.00. In fact, the Poisson's ratio larger than 1.00 is allowed in this 2D structure. For 2D systems with a square lattice, the elastic constants C_{11} and C_{22} are equivalent. The Born–Huang criteria in these systems (specifically, $C_{11} > |C_{12}|$)[42] guarantee $C_{12}/C_{11} = C_{12}/C_{22} < 1$, leading to a Poisson's ratio of less than 1.00 along the [100] and [010] directions. However, for 2D systems with a rectangular lattice, the Born–Huang criteria can be expressed as $C_{11}C_{22} > C_{12}^2$,[42] and the non-equivalent C_{11} and C_{22} lead to non-identical C_{12}/C_{11} and C_{12}/C_{22} values. As a result, one of the axial Poisson's ratios can be larger than 1.00 without violating the Born–Huang criteria.

A comparison of the Poisson's ratio values of penta-BCP and some other 2D materials is listed in Table 1. There are many

Table 1 Comparison of the largest value of Poisson's ratio (ν) of penta-BCP with that of some other 2D materials

Structure	ν	Direction
Penta-BCP	1.30	[010]
Penta-C$_2$B$_4$[50]	0.906	[100] and [010]
Penta-BCN[16]	0.026	[010]
Penta-CNP[17]	0.025	[100] and [010]
Penta-BNSi[37]	0.11	[110]
GeSe$_2$[47]	1.20	[010]
ScP[48]	1.261	[100]
YSb[48]	1.101	[100]
YBi[48]	1.054	[100]
α-Arsenene[49]	1.07	[010]
Four-layered arsenene[49]	1.19	[010]

non-pentagon-based 2D sheets with their Poisson's ratio greater than 1.00, for instance, GeSe$_2$ (1.20, [010]),[47] ScP (1.261, [100]),[48] YSb (1.101, [100]),[48] YBi (1.054, [100]),[48] α-arsenene (1.07, [010]),[49] and four-layered arsenene (1.19, [010]),[49] while penta-BCP is the first penta-sheet that exhibits a Poisson's ratio larger than 1.0 along the [010] direction, which is much higher than the value of 0.026 in pristine penta-BCN[16] and even higher than the previous record for a high Poisson's ratio in the pentagon-based sheets held by penta-C$_2$B$_4$ (0.906).[50] It is also worth mentioning that the Poisson's ratio of penta-BCP has a negative value of −0.28 for $\theta = 48°$ and its equivalents. The absolute value is larger than that of penta-CNP (−0.04)[17] and penta-SiCN (−0.132),[38] which shows its potential application in nanomechanical devices as a nano-auxetic material. Because the in-plane projections of C–B and C–P bonds are close to the [110] direction and its equivalents, the values of both $\theta_1(B_1–C–P_1)$ and $\theta_2(B_2–C–P_2)$ increase with tensile strain applied along the [110] direction. This leads to the expansion in the transverse direction at $\theta = 48°$ and its equivalents, thus, resulting in the negative Poisson's ratio.

3.3 Electronic properties

The electronic properties of penta-BCP are studied by calculating the electronic band structure, total density of states (DOS) and atomic projected DOS (PDOS). As shown in Fig. 4(a), penta-BCP is semiconducting with an indirect band gap of 1.97 eV at
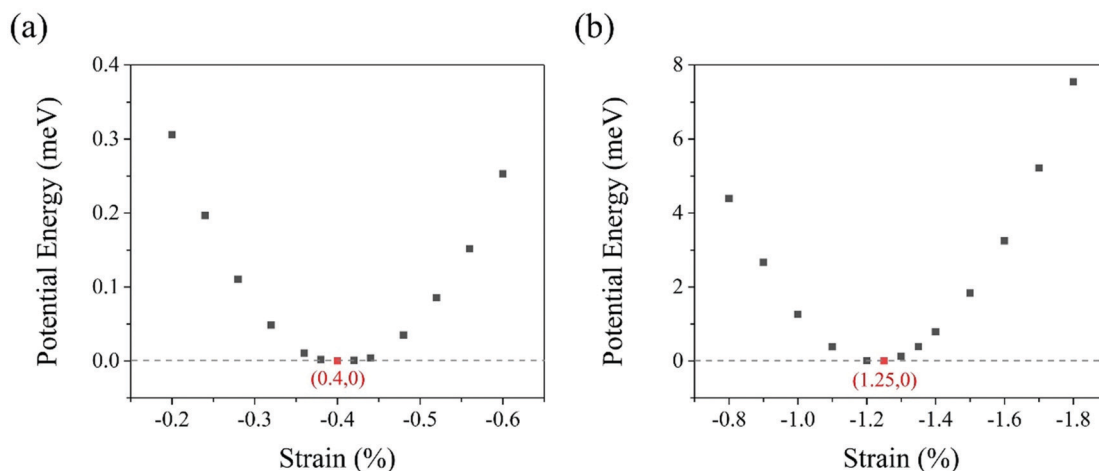

Fig. 3 Variation of the potential energy of penta-BCP with lateral strain under tensile strain of 1.00% along (a) the [100] and (b) [010] directions.

This journal is © The Royal Society of Chemistry 2022

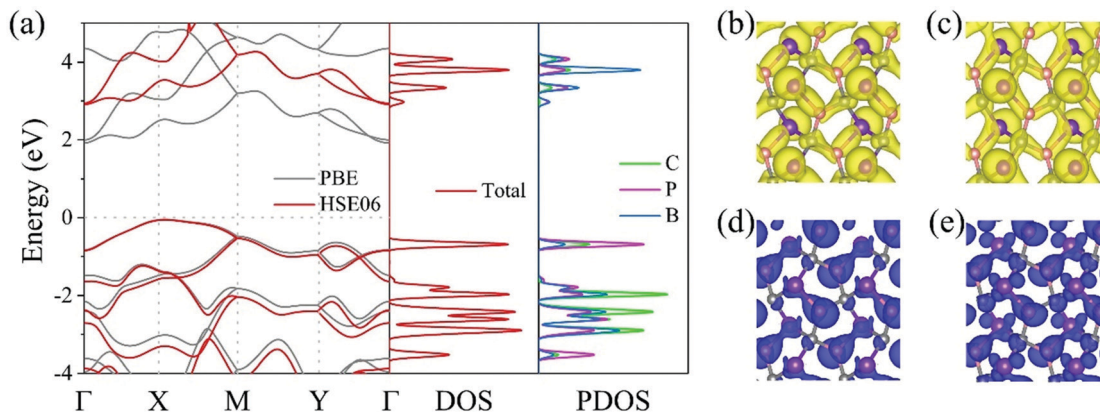*J. Mater. Chem. C*, 2022, **10**, 10302–10309 | **10305**

Fig. 4 (a) Electronic band structure, DOS, and PDOS of penta-BCP. Band-decomposed charge-density distribution of (b) the second highest occupied band, (c) the highest occupied band, (d) the lowest unoccupied band, and (e) the second lowest unoccupied band of penta-BCP (isosurface values = 0.008 Å^{-3}).

the PBE level, as the valence band maximum (VBM) and the conduction band minimum (CBM) are located at the high-symmetry points X and Γ in the first Brillouin zone, respectively. The electronic band structure at the HSE06 level has a similar dispersion but a wider band gap of 2.97 eV compared with that at the PBE level due to the well-known fact that the PBE functional underestimates band gaps. From the PDOS in Fig. 4(a), one can see that the VBM is mainly contributed by the P atoms, while the CBM mainly comes from the B and P atoms. As shown in the band-decomposed charge-density distributions in Fig. 4(b–e), the contributions to the electronic states of the P and B atoms near the Fermi level are consistent with the PDOS results. In addition, the charge-density distributions are asymmetrical, leading to spontaneous polarization in penta-BCP.

3.4 Spontaneous polarization

In order to generate spontaneous polarization in a 2D material, the chemically equivalent polarized bonds should be arranged in a configuration where their local polarizations cannot cancel out, so that the centers of positive and negative charge can be separated. Such a configuration is forbidden in the highly symmetric hexagonal, tetragonal and orthorhombic 2D

structures constructed by the corresponding motifs. By comparison, a spontaneous polarization along the [010] direction is allowed due to the monoclinic symmetry of penta-BCP. Based on Berry phase theory, the spontaneous polarization of penta-BCP is quantified by calculating the dipole moment using the finite electric field method,[35] which is shown below:

$$P_{\rm s} = P_{\rm s}^{\rm ion} + P_{\rm s}^{\rm ele} \tag{3}$$

$$P_{\rm s}^{\rm ion} = \frac{|e|}{\Omega} \sum_{i=1}^{N_{\rm atom}} Z_i^V \Delta ri \tag{4}$$

where $P_{\rm s}$, $P_{\rm s}^{\rm ion}$, and $P_{\rm s}^{\rm ele}$ are the total polarization, the ionic contribution, and the electronic contribution, respectively, Ω is the volume of the unit cell, and $|e|Z_i^V$ and Δr_i represent the valence charge and the displacement of the i-th atom, respectively.

The spontaneous polarization of penta-BCP is calculated to be 4.66×10^{-10} C m^{-1}, which is larger than that of penta-BCN (3.17×10^{-10} C m^{-1}) and penta-CNP (4.33×10^{-10} C m^{-1}).[16,17] The results of Bader charge analysis[51,52] in Fig. 5(a) show that each C atom gains 1.89 electrons from its neighboring B and P atoms, while each B and P atom contributes 1.43 and 0.46
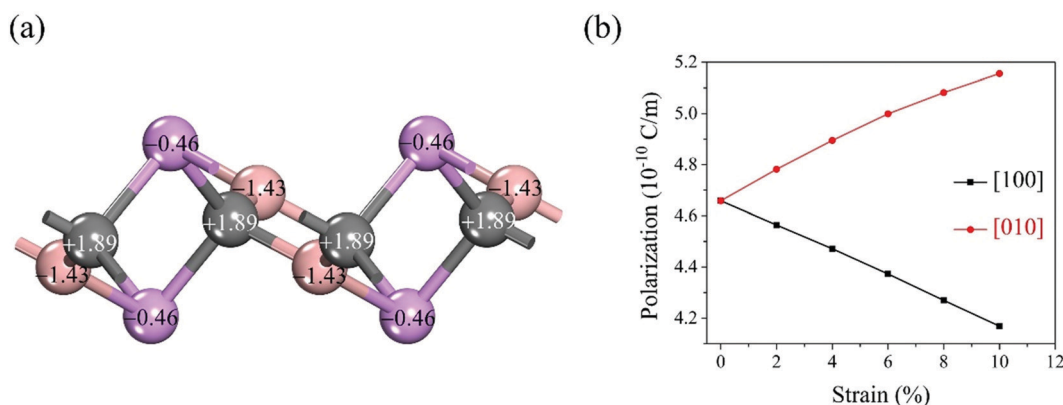

Fig. 5 (a) Bader charge distribution on the atoms in penta-BCP, and (b) polarization of penta-BCP with 2%, 4%, 6%, 8%, and 10% uniaxial tensile strain along the [100] and [010] directions.

electrons, respectively. The intensities of electron transfer can be explained by the electronegativity of these elements. The electronegativity of P (2.19) falls in between that of B (2.04) and C (2.55). Thus, C gains more electrons from B than from P. The atomic charges demonstrate the highly polarized nature of the C–B, C–P, and B–P bonds, and the polarization of these bonds adds up in the [010] direction whereas it cancels out along the [100] and out-of-plane directions, leading to a spontaneous polarization along the [010] direction in penta-BCP. The most highly polarized bond in this structure is the C–B bond between the four-fold coordinated C and the three-fold coordinated B, which is different from the most highly polarized B–N and N–P bond between the three-fold coordinated atoms in penta-BCN and penta-CNP. The C–B bond is closer to the [010] direction than the B–N and N–P bonds, thus, the spontaneous polarization of penta-BCP is 4.66×10^{-10} C m^{-1}, larger than that of pristine penta-BCN (3.17×10^{-10} C m^{-1}) and penta-CNP (4.33×10^{-10} C m^{-1}). In addition, we apply 2%, 4%, 6%, 8%, and 10% uniaxial tensile strain along the [100] or [010] directions, the results of which are shown in Fig. 5(b) (detailed information and phonon dispersions of penta-BCP under 10% uniaxial tensile strain are presented in Table S1 and Fig. S4 in the ESI,† respectively). It is found that the spontaneous polarization of penta-BCP increases with the uniaxial tensile strain along the [010] direction but decreases with the uniaxial tensile strain along the [100] direction. This can be explained by the configuration of the most heavily polarized C–B bond in penta-BCP. The bond axis of the C–B bond shifts closer to the [010] direction under uniaxial tensile strain along the [010] direction, and it deviates from the [010] direction under uniaxial tensile strain along the [100] direction.

3.5 Intrinsic piezoelectricity

The semiconducting feature and large spontaneous polarization in the non-centrosymmetric configuration of penta-BCP give rise to a strong piezoelectric response. Due to the constraints of lattice symmetry of penta-BCP, the relationship between the piezoelectric stress tensor, the piezoelectric strain tensor, and the linear elastic constants can be presented as below:[53,54]

$$
\begin{pmatrix} 0 & 0 & e_{16} \\ e_{21} & e_{22} & 0 \\ 0 & 0 & e_{36} \end{pmatrix} = \begin{pmatrix} 0 & 0 & d_{16} \\ d_{21} & d_{22} & 0 \\ 0 & 0 & d_{36} \end{pmatrix} \begin{pmatrix} C_{11} & C_{12} & 0 \\ C_{12} & C_{22} & 0 \\ 0 & 0 & C_{66} \end{pmatrix}
$$

$$(5)$$

From eqn (5), eqn (6)–(9) are derived which describe the relationship between the non-zero independent piezoelectric strain coefficients and piezoelectric stress coefficients. The calculated results are listed in Table 2, and the piezoelectric responses of some other previously reported 2D sheets are listed in Table 3 for comparison. The positive and negative values of the piezoelectric coefficients correspond to the positive and negative directions of the axial dipole moments

Table 2 Piezoelectric stress tensor e_{ij} (in 10^{-10} C m^{-1}), and piezoelectric strain tensor d_{ij} (in pm V^{-1}) of penta-BCP

Parameter			
e_{21}	e_{22}	e_{16}	e_{36}
−2.53	1.35	−1.00	0.35
d_{21}	d_{22}	d_{16}	d_{36}
−13.57	6.33	−1.31	0.46

Table 3 Comparison of the piezoelectric coefficients e and d of penta-BCP with those of some other 2D materials

Structure	e (10^{-10} C m^{-1})	d (pm V^{-1})
Penta-BCP	−2.53 (e_{21}), 1.35 (e_{22})	−13.57 (d_{21}), 6.33 (d_{22}),
Penta-BCN[16]	1.93 (e_{21}), −1.24 (e_{22})	0.878 (d_{21}), −0.678 (d_{22})
Penta-CNP[17]	2.37 (e_{21}), −1.21 (e_{22})	1.39 (d_{21}), −0.69 (d_{22})
Penta-BNSi[37]	3.78 (e_{21}), −2.40 (e_{22})	3.59 (d_{21}), −2.57 (d_{22})
h-BN[3]	1.38 (e_{11})	0.60 (d_{11})
F-InN-H[55]	2.42 (e_{11})	9.02 (d_{11})

generated by the external tensile strain, respectively.

$$d_{16} = \frac{e_{16}}{C_{66}} \quad (6)$$

$$d_{21} = \frac{C_{21}e_{22} - C_{22}e_{21}}{C_{21}C_{12} - C_{11}C_{22}} \quad (7)$$

$$d_{22} = \frac{C_{12}e_{21} - C_{11}e_{22}}{C_{21}C_{12} - C_{11}C_{22}} \quad (8)$$

$$d_{36} = \frac{e_{36}}{C_{66}} \quad (9)$$

The in-plane piezoelectric response d_{21} of penta-BCP (−13.57 pm V^{-1}) is the strongest among the non-zero components, which is an order of magnitude larger than those of penta-BCN, penta-CNP, and penta-BNSi, and is larger than those of the Janus hydrofluorinated InN.[55] It is also worth mentioning that the lateral tensile strain along different directions contributes to an overall piezoelectric response. Interestingly, due to the large positive Poisson's ratio of penta-BCP, tensile strain along the [010] direction can generate an equally significant compressive strain along the [100] direction, corresponding to the piezoelectric strain tensor components d_{22} and d_{21}. The overall piezoelectric response induced by the coupling of piezoelectricity and Poisson's ratio can be expressed by

$$d^{\text{eff}} \times \varepsilon_i = d_{ki} \times \varepsilon_i \times d_{kj} \times \varepsilon_j \quad (10)$$

$$d^{\text{eff}} = d_{ki} - d_{kj} \times \nu_i \quad (11)$$

where d^{eff} is the overall piezoelectric response, ε_i and ε_j are strains that are perpendicular to each other induced by Poisson's ratio of ν_i, and d_{ki} and d_{kj} are the piezoelectric response induced by the corresponding strain. The dipole moments caused by the two strains point toward the same direction,

This journal is © The Royal Society of Chemistry 2022

J. Mater. Chem. C, 2022, **10**, 10302–10309 | **10307**

i.e., positive tensile strain along the [010] direction $\times$ positive d_{22}, and negative lateral compressive strain along the [100] direction $\times$ negative d_{21}. Thus, the two piezoelectric responses add up to each other in the [010] direction, resulting in an enhanced overall piezoelectric response of -16 pm V^{-1} and 24 pm V^{-1} with respect to tensile strain along the [100] and [010] directions, which are 17.91% and 279% larger than the piezoelectric strain tensor components d_{21} and d_{22}, respectively. For comparison, after considering the coupling of piezoelectricity and Poisson's ratio, the overall piezoelectric response of penta-BCN, penta-CNP, and penta-BNSi are only increased by no more than 3.4%, 5%, and 15.4%, respectively, because they have low Poisson's ratio values along the axial directions.

4. Conclusions

Based on first-principles calculations, we have proposed a new ternary pentagon-based sheet, penta-BCP, which is dynamically, thermally, and mechanically stable. It is semiconducting with an indirect band gap of 2.97 eV, and possesses several intriguing properties: (1) penta-BCP is the first pentagon-based sheet with a Poisson's ratio larger than 1.00, with a record high value of 1.30 along the [010] direction in all pentagon-based 2D materials; (2) penta-BCP possesses strong piezoelectricity, which is the largest among the pentagon-based sheets that consist of light elements reported so far; and (3) the large piezoelectric coefficients, together with the large axial Poisson's ratio, lead to a significantly enhanced overall piezoelectric response of 24 pm V^{-1} with respect to tensile strain along the [010] direction. Therefore, this material is promising for application in piezoelectric devices. Our work demonstrates that multi-component penta-sheets provide a special platform for the design of multi-functional materials.

Conflicts of interest

The authors declare no competing financial interest.

Acknowledgements

References

1 W. Wu, L. Wang and Y. Li, *et al.*, Piezoelectricity of single-atomic-layer MoS$_2$ for energy conversion and piezotronics, *Nature*, 2014, **514**(7523), 470–474.

2 M. Yang, Z. Luo and Z. Mi, *et al.*, Piezoelectric and pyroelectric effects induced by interface polar symmetry, *Nature*, 2020, **584**(7821), 377–381.

3 K. Duerloo, M. Ong and E. Reed, Intrinsic piezoelectricity in two-dimensional materials, *J. Phys. Chem. Lett.*, 2012, **3**(19), 2871–2876.

4 M. Bykov, E. Bykova and A. Ponomareva, *et al.*, Realization of an ideal cairo tessellation in nickel diazenide NiN$_2$: High-pressure route to pentagonal 2D materials, *ACS Nano*, 2021, **15**(8), 13539–13546.

5 S. Zhang, J. Zhou and Q. Wang, *et al.*, Penta-graphene: A new carbon allotrope, *Proc. Natl. Acad. Sci. U. S. A.*, 2015, **112**(8), 2372–2377.

6 X. Li, Y. Dai and W. Wei, *et al.*, Stable Si-based pentagonal monolayers: High carrier mobilities and applications in photocatalytic water splitting, *J. Mater. Chem. A*, 2015, **3**(47), 24055–24063.

7 Y. Ding and Y. Wang, Hydrogen-induced stabilization and tunable electronic structures of penta-silicene: A computational study, *J. Mater. Chem. C*, 2015, **3**(43), 11341–11348.

8 S. Qian, X. Sheng and X. Xu, *et al.*, Penta-MX$_2$ (M = Ni, Pd and Pt; X = P and As) monolayers: Direct band-gap semiconductors with high carrier mobility, *J. Mater. Chem. C*, 2019, **7**(12), 3569–3575.

9 M. Debbichi, A. Mallah and M. Dhaou, *et al.*, First-principles study of monolayer penta-CoS$_2$ as a promising anode material for Li/Na-ion batteries, *Phys. Rev. Appl.*, 2021, **16**(2), 024016.

10 M. Debbichi and A. Alhodaib, Stability, electronic and magenetic properties of the penta-CoAsSe monolayer: A first-principles and monte carlo study, *Phys. Chem. Chem. Phys.*, 2022, **24**(9), 5680–5689.

11 J. Cerda, J. Slawinska and G. Lay, *et al.*, Unveiling the pentagonal nature of perfectly aligned single-and double-strand Si nano-ribbons on Ag(100), *Nat. Commun.*, 2016, **7**(1), 13076.

12 A. D. Oyedele, S. Yang and L. Liang, *et al.*, PdSe$_2$: Pentagonal two-dimensional layers with high air stability for electronics, *J. Am. Chem. Soc.*, 2017, **139**(40), 14090–14097.

13 H. J. Jia, H. M. Mu and J. P. Li, *et al.*, Piezoelectric and polarized enhancement by hydrofluorination of penta-graphene, *Phys. Chem. Chem. Phys.*, 2018, **20**(41), 26288–26296.

14 L. Liu and H. L. Zhuang, Single-layer ferromagnetic and piezoelectric CoAsS with pentagonal structure, *APL Mater.*, 2019, **7**(1), 011101.

15 S. Guo and S. Wang, Tuning pure out-of-plane piezoelectric effect of penta-graphene: A first-principle study, *J. Phys. Chem. Solids*, 2020, **140**, 109375.

16 K. Zhao, Y. Guo and Y. Shen, *et al.*, Penta-BCN: A new ternary pentagonal monolayer with intrinsic piezoelectricity, *J. Phys. Chem. Lett.*, 2020, **11**(9), 3501–3506.

17 W. Sun, Y. Shen and Y. Guo, *et al.*, 1,2,4-Azadiphosphole-based piezoelectric penta-CNP sheet with high spontaneous polarization, *Appl. Surf. Sci.*, 2021, **554**, 149499.

18 Y. Shen and Q. Wang, Pentagon-based 2D materials: classification, properties and applications, *Phys. Rep.*, 2022, **964**, 1–42.

19 Y. Guo, C. Zhang and J. Zhou, *et al.*, Lattice dynamic and instability in pentasilicene: A light single-element ferroelectric

material with high Curie temperature, *Phys. Rev. Appl.*, 2019, **11**(6), 064063.

20 R. Hinchet, U. Khan and C. Falconi, *et al.*, Piezoelectric properties in two-dimensional materials: Simulations and experiments, *Mater. Today*, 2018, **21**(6), 611–630.

21 S. Rajala, T. Siponkoski and E. Sarlin, *et al.*, Cellulose nanofibril film as a piezoelectric sensor material, *ACS Appl. Mater. Interfaces*, 2016, **8**(24), 15607–15614.

22 A. Halliyal, A. Safari and A. S. Bhalla, *et al.*, Grain-oriented glass-ceramics for piezoelectric devices, *J. Am. Ceram.*, 1984, **67**(5), 331–335.

23 J. Yuan and K. M. Liew, Effects of boron nitride impurities on the elastic properties of carbon nanotubes, *Nanotechnology*, 2008, **19**(44), 445703.

24 J. M. Martin, C. Grossiord and K. Varlot, Synergistic effects in binary systems of lubricant additives: A chemical hardness approach, *Tribol. Lett.*, 2000, **8**(4), 193–201.

25 G. Kresse and J. Furthmüller, Efficient iterative schemes for ab initio total-energy calculations using a plane-wave basis set, *Phys. Rev. B*, 1996, **54**(16), 11169–11186.

26 P. E. Blöchl, Projector augmented-wave method, *Phys. Rev. B*, 1994, **50**(24), 17953–17979.

27 J. P. Perdew, K. Burke and M. Ernzerhof, Generalized gradient approximation made simple, *Phys. Rev. Lett.*, 1996, **77**(18), 3865–3868.

28 J. Heyd and G. E. Scuseria, Assessment and validation of a screened coulomb hybrid density functional, *J. Chem. Phys.*, 2004, **120**(16), 7274–7280.

29 H. J. Monkhorst and J. D. Pack, Special points for Brillouin-zone integrations, *Phys. Rev. B*, 1976, **13**(12), 5188–5192.

30 K. Parlinski, Z. Q. Li and Y. Kawazoe, First-principles determination of the soft mode in cubic ZrO_2, *Phys. Rev. Lett.*, 1997, **78**(21), 4063–4066.

31 A. Togo and I. Tanaka, First principles phonon calculations in materials science, *Scr. Mater.*, 2015, **108**, 1–5.

32 D. Bucher, L. C. T. Pierce and J. A. McCammon, On the use of accelerated molecular dynamics to enhance configurational sampling in ab initio simulations, *J. Chem. Theory Comput.*, 2011, **7**(4), 890–897.

33 C. Braga and K. P. A. Travis, A configurational temperature nose-hoover thermostat, *J. Chem. Phys.*, 2005, **123**(13), 134101.

34 X. Wu, D. Vanderbilt and D. R. Hamann, Systematic treatment of displacements, strains, and electric fields in density-functional perturbation theory, *Phys. Rev. B*, 2005, **72**(3), 035105.

35 R. D. King-Smith and D. Vanderbilt, Theory of polarization of crystalline solids, *Phys. Rev. B*, 1993, **47**(3), 1651–1654.

36 S. Baroni, S. de Gironcoli and A. Dal Corso, *et al.*, Phonons and related crystal properties from density-functional perturbation theory, *Rev. Mod. Phys.*, 2001, **73**(2), 515–562.

37 M. J. Varjovi, M. E. Kolic and E. Durgun, Ternary pentagonal BNSi monolayer: Two-dimensional structure with potentially high carrier mobility and strong excitonic effects for photocatalytic applications, *Phys. Rev. Mater.*, 2022, **6**(3), 034004.

38 S. B. Sharma, I. A. Qattan and M. Jaishi, *et al.*, Penta-SiCN: A highly auxetic monolayer, *ACS Appl. Electron. Mater.*, 2022, **4**(5), 2561–2569.

39 E. Balcı, Ü. Ö. Akkuş and S. Berber, BPC_2: Graphene-like ternary semi-metal material, *Phys. E*, 2019, **107**, 5–10.

40 V. Kumar, K. Rajput and D. R. Roy, Electric field-induced band modulation of predicted ternary 2D MXC_3 [M:X = As:Ge, Sb:Sn and Bi:Pb] with strong stability and optical properties, *Carbon*, 2021, **172**, 791–803.

41 N. S. Abraham and M. R. Shirts, Thermal gradient approach for the quasi-harmonic approximation and its application to improved treatment of anisotropic expansion, *J. Chem. Theory Comput.*, 2018, **14**(11), 5904–5919.

42 R. C. Andrew, R. E. Mapasha and A. M. Ukpong, Mechanical properties of graphene and boronitrene, *Phys. Rev. B*, 2012, **85**(12), 125428.

43 E. Cadelano, P. L. Palla and S. Giordano, *et al.*, Elastic properties of hydrogenated graphene, *Phys. Rev. B*, 2010, **82**(23), 235414.

44 J. W. Jiang and H. S. Park, Mechanical properties of single-layer black phosphorus, *J. Phys. D*, 2014, **47**(38), 385304.

45 C. Lee, X. Wei and J. W. Kysar, *et al.*, Measurement of the elastic properties and intrinsic strength of monolayer graphene, *Science*, 2008, **321**(5887), 385–388.

46 S. Bertolazzi, J. Brivio and A. Kis, Stretching and breaking of ultrathin MoS_2, *ACS Nano*, 2011, **5**(12), 9703–9709.

47 Z. Chen, Z. Li and H. Wang, Two-dimensional auxetic $GeSe_2$ material with ferroelasticity and flexoelectricity, *J. Phys. Chem. C*, 2021, **125**(36), 19666–19672.

48 J. H. Yuan, G. Q. Mao and K. H. Xue, *et al.*, A new family of two-dimensional ferroelastic semiconductors with negative Poisson's ratios, *Nanoscale*, 2020, **12**(26), 14150–14159.

49 J. Han, J. Xie and Z. Zhang, *et al.*, Negative Poisson's ratios in few-layer orthorhombic arsenic: first-principles calculations, *Appl. Phys. Express*, 2015, **8**(4), 041801.

50 Z. Cheng, X. Zhang and H. Zhang, *et al.*, Binary pentagonal auxetic materials for photocatalysis and energy storage with outstanding performances, *Nanoscale*, 2022, **14**, 2041–2051.

51 G. Henkelman, A. Arnaldsson and H. Jónsson, A fast and robust algorithm for bader decomposition of charge density, *Comput. Mater. Sci.*, 2006, **36**(3), 354–360.

52 W. Tang, E. Sanville and G. Henkelman, A grid-based bader analysis algorithm without lattice bias, *J. Phys.: Condens. Matter*, 2009, **21**(8), 084204.

53 H. Ghasemi, H. S. Park and T. Rabczuk, A level-set based IGA formulation for topology optimization of flexoelectric materials, *Comput. Methods Appl. Mech. Eng.*, 2017, **313**, 239–258.

54 H. V. Do, T. Lahmer and X. Zhuang, *et al.*, An isogeometric analysis to identify the full flexoelectric complex material properties based on electrical impedance curve, *Comput. Struct.*, 2019, **214**, 1–14.

55 Y. Guo, H. Zhu and Q. Wang, Piezoelectric effects in surface-engineered two-dimensional group III nitrides, *ACS Appl. Mater. Interfaces*, 2019, **11**(1), 1033–1039.

This journal is © The Royal Society of Chemistry 2022

J. Mater. Chem. C, 2022, **10**, 10302–10309 | **10309**